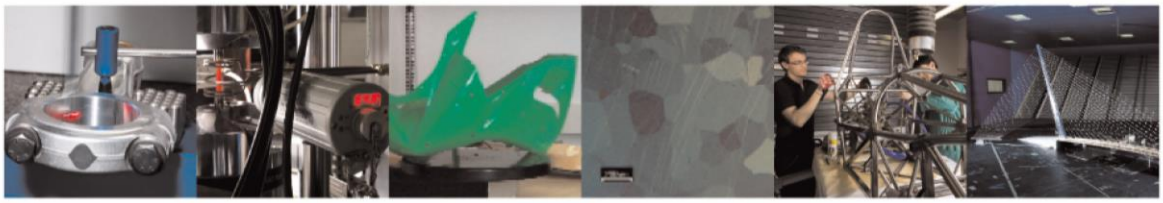

# Single point exposure LPBF for the production of biodegradable Zn-alloy lattice structures

Guaglione F.; Caprio L.; Previtali B.; Demir A.G.

This is a post-peer-review, pre-copyedit version of an article published in Additive Manufacturing. The final authenticated version is available online at:
http://dx.doi.org/10.1016/j.addma.2021.102426



DIPARTIMENTO DI MECCANICA ■ POLITECNICO DI MILANO
via G. La Masa, 1 ■ 20156 Milano ■ EMAIL (PEC): pecmecc@cert.polimi.it
http://www.mecc.polimi.it
Rev. 0

# Single point exposure LPBF for the production of biodegradable Zn-alloy lattice structures

Fabio Guaglione[1], fabio.guaglione@mail.polimi.it

Leonardo Caprio[1], leonardo.caprio@polimi.it

Barbara Previtali[1], barbara.previtali@polimi.it

Ali Gökhan Demir[1,*], aligokhan.demir@polimi.it

[1]Department of Mechanical Engineering, Politecnico di Milano, Via La Masa 1, 20156 Milan, Italy

*Corresponding author: aligokhan.demir@polimi.it

**Single point exposure LPBF for the production of biodegradable Zn-alloy lattice structures**

Fabio Guaglione[1], Leonardo Caprio[1], Barbara Previtali[1], Ali Gökhan Demir[1,*]

[1]Department of Mechanical Engineering, Politecnico di Milano, Via La Masa 1, 20156 Milan, Italy

*Corresponding author: aligokhan.demir@polimi.it

## Abstract

The processing of Zn alloys through Laser Powder Bed Fusion (LPBF) with conventional vector-based scan strategies poses significant challenges regarding process stability. The evaporation tendency of such materials limits the quality of the process outcome introducing excessive porosity and low geometrical accuracy. Commonly, this issue requires a modification on the hardware of the LPBF machine employed concerning the gas management. The process instability and excessive vapour generation can be avoided also a careful control of the laser energy deposited over time. Hence, this study focuses on the novel scan strategies ad a possible solution. Single Point Exposure (SPE) scan strategy was applied to process Zn-0.5Mg powders, allowing to suppress the excessive smoke formation in the printing of body centred cubic (BCC) cell lattice structures. The new strategy was developed via an open LPBF system, together with dedicated slicing software for laser path and parameter assignment. The laser pulse profiles were characterized with a fast photodiode in the SPE control mode. Lattices with strut diameters smaller than 200 μm could be obtained, proving the capability of the strategy in the processing of fine features on challenging materials such as Zn alloys maintaining process stability. The lattice struts were adequately densified without excessive porosity and the relative density of the lattices were controlled between 2-35% by means of the process parameters and cell size. The obtained samples were also characterized regarding their mechanical properties, showing controllable stiffness of the lattices as prospect materials load-bearing biodegradable implants.

**Keywords:** Biodegradable metals; Single point exposure, Zinc, Lattice structure

# 1 Introduction

In the last years, the interest in Additive Manufacturing (AM) applied to biodegradable porous metal implants has seen a significant growth, mostly due to its capability to produce highly customized structures in terms of macro and microgeometry with reduced lead times [1,2]. Especially, Laser Powder Bed Fusion (LPBF) technology is arguably the most advanced AM technology for producing customized metal implants. An appealing application for these structures is bone scaffolds. Artificial bone grafting should provide a favourable structure for bone cell adhesion and proliferation, leading to bone ingrowth [3]. Such implants, rely on specific requirements regarding the microgeometry (interconnected pores with suitable geometry) [4], macro geometry (patient-specific) and mechanical properties [5]. Especially, regarding pore size of the designed structure, the minimum value to allow angiogenesis is 100 µm while a pore size in the 300-900 µm range is considered beneficial for bone ingrowth [5]. Additionally, an appealing property for the next-generation customized implants is biodegradability of the material, to enable the reabsorption of the implants in the host body [6] [7]. Commonly investigated materials are Fe and Mg alloys, but Zn alloys represent an emerging trend thanks to the favourable degradation rate [8], biocompatibility and osteogenic potential [9][10]. Compressive strength of the bone lies in the 90-205 MPa and 0.1-14 MPa range, while Young's Modulus lies in the 1-35 GPa and 0.1-1.4 GPa respectively for cortical and cancellous bone [3].

Previous works investigating the processability of Zn alloys through LPBF have evidenced severe issues connected to the evaporation tendency of the material caused by the low melting and boiling point, leading in turn to process instability and high levels of porosity [11,12]. During the laser based processing of Zn employing conventional Gaussian-like beam distributions, the boiling is expected to occur at the central part of the irradiation point. As the boiling continues progress the Zn vapour is expected exert recoil pressure on the melt pool, pushing it downwards progressing towards a keyhole regime and increasing the penetrated depth by the laser beam. Resultantly keyhole pores, gas entrapment and powder bed denudation can occur [13]. To address the issue, hardware solutions have been used to compensate for the excessive evaporation with a specially designed, enhanced recirculation system while maintaining the conventional vector-based scan strategies (e.g. contour-hatch) [14,15]

Demir et al. managed to obtain a stable LPBF processing of pure Zn bulk samples in an open chamber with an inert gas jet flow over the powder bed [14]. Lietaert et al. carried on a similar work, where a proper recirculation system and the optimization of process parameters allowed to obtain dense pure Zn bulk samples [16]. Chen et al. studied and designed a gar recirculation system specifically tailored for the LPBF of prone to evaporation materials managing to print with an optimal density pure Zn cubes [17]. The same custom-made system has been used by Wen et al. to fabricate pure Zn cardiovascular stents and porous scaffolds [15,18]. All these works involved vector-based scan strategies and required a hardware modification. The difficulty of processing Zn and its alloys by LPBF limited also the studies on different alloy types and geometries. Improving processing conditions by the control of the laser emission profile is an appealing aspect also to open up further work on newer alloys for comparing their mechanical and biological performance with respect to those produced by conventional manufacturing processes.

Conventional LPBF scan strategies rely on consecutive line scan by a fast moving laser beam to selectively melt the powder bed where required in each single layer, leading to possible time-dependent thermal build up and to a sub-optimal resolution when dealing with fine structures. Commonly, continuous wave (CW) emission is used with such vector-based scan strategies. The choice of the correct scan strategy is fundamental for the geometrical fidelity, surface roughness, internal defects and the mechanical properties of the lattice structures [19,20]. On the other hands, studies have shown the potentiality of pulsed wave (PW) emission to obtain a finer resolution of the tool [21], and to control the energy release and melt pool formation more flexibly [22]. The use of pulsed wave emission has been shown to be effective for producing highly detailed cardiovascular stents [23–25] as well as porous structures for biodegradable orthopaedic implants [26]. Nonetheless, the majority of the literature sources refer to vector-based scan strategies, even regarding difficult to process materials such as Zn alloys.

An alternative is represented by Single Point Exposure (SPE) scan strategy. Such strategy consists in the positioning of the laser beam at precise locations subsequently exposed by means of a single laser pulse characterized by a certain duration and laser power. The strategy is capable of exploiting the components of standard industrial LPBF machines to perform a novel processing on the material. The galvanometric mirrors are used for the positioning of the laser beam at the predetermined locations, then stopped while the laser source is

modulated in order to obtain therein the exposure of the powder bed to a single laser pulse. SPE has been previously applied to conventional LPBF materials such as Ti alloys and AISI316L [27–30]. While its use for improving the process resolution has been discussed for these materials, to the authors' knowledge its use for an enhanced control on the consolidation of the materials with low processability has not been addressed. Concerning the biodegradable Zn-alloys, the use PSE can provide two main advantages: i- suppressing the excessive vapour formation leading to process instability, and ii- reducing the processed strut size in lattice structures for a greater control of the mechanical and biodegradation behaviour. As a matter of fact, SPE can be applied to conventional LPBF systems by adjusting the laser control software without the necessity to intervene with the hardware, rendering this approach highly desirable for future applications.

In this work, Single Point Exposure strategy has been employed for a smoke-free production of Zn-0.5Mg body centered Cubic (BCC) lattice structures with LPBF. An open industrial LPBF system equipped with a conventional single mode fiber laser and scanner optics was used with a customized laser trajectory and parameter assignment software. The effect of the SPE control parameters on the laser emission profile was first characterized. An experimental study was conducted using these parameters to produce lattices with different cell sizes. The produced samples were characterized to assess their density, geometry, as well as compressive strength. Finally, a mock-up biodegradable facial implant with a conformal shape was produced demonstrating the capacity of the newly developed LPBF strategy.

## 2 Single Point Exposure functioning principle for producing lattice structures

Single Point Exposure, being a non-conventional scan strategy based on points instead of linear vectors, needs the definition of the process parameters involved in the melting and consolidation process. As previously briefly described, during SPE the laser beam is positioned at specific locations where single laser pulses are emitted. Laser pulses are characterized by a certain duration ($t_{on}$) and by a peak laser power ($P$) similar to what occurs in pulsed wave emission [31]. The pulse duration is in the µs range, obtained through a fast modulation of a continuous wave (CW) fiber laser source. Hence, considering the typical delays and rise times for commercial CW fiber laser sources, the single pulse shape can be approximated with a square wave and $P$ can be regarded as the laser emission

power reached for a duration equal to $t_{on}$. With conventional CW fiber laser sources, controlled via analogue and digital signals, $P$ would be set through the analogue channel, while the $t_{on}$ would be consequent to the modulation operated through the digital signal. Regarding the pulse duration, a proper calibration is needed in order to compensate for the typical delays between digital signal and actual laser emission. The combination of the pulse parameters influences the melting dynamics during the process and the thickness of the obtained features. As a consequence to each pulse, a circular melt pool with a certain diameter will be created. A visual representation of the single pulse interaction is provided in Figure 1. The energetic input, as with conventional strategies, should be optimized in order to be sufficient to melt the material while avoiding its vaporization, especially with evaporation-prone alloys, such as Zn ones.

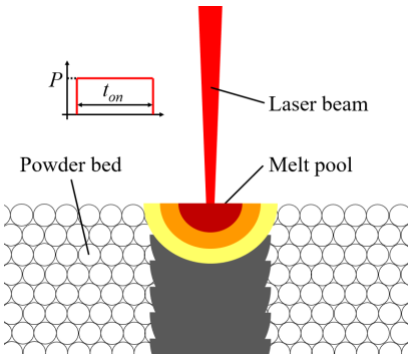


**Figure 1.** Schematic representation of the single pulse interaction

In order to produce 3D parts, the laser trajectory and the exposure points should be calculated in a layer-by-layer fashion. Single pulse locations should be defined for each layer in terms of x and y coordinates according to the geometry to be obtained. A simple approach to the issue is the definition of such locations taking as an input a conventional CAD file, performing the slicing, and subsequently defining the locations as centroids of the 2D surfaces obtained with the slicing process. This approach, namely "centroid-defined SPE", is valid for filigree structures where the sections resulting from the slicing process involve near-circular shapes. An example of such approach applied to a BCC lattice structure, which will be the geometry involved for the present work. Figure 2 describes the production of a bone porous implant mock-up based on an existing bone defect on a model jawbone. The missing bone volume is reconstructed as a 3D CAD file. Then, BCC lattice structure with is generated inside the volume with a chosen unitary cell dimension $c$. The dedicated CAM software performs the slicing on the lattice

geometry. For each slice, the closed contours are found and their centroid locations are calculated. At each centroid location a single pulse is to be released with a determined pulse duration and power. The manufacturing phases follow the conventional LPBF process, where after each layer the powder bed is lowered by the layer thickness ($z$).

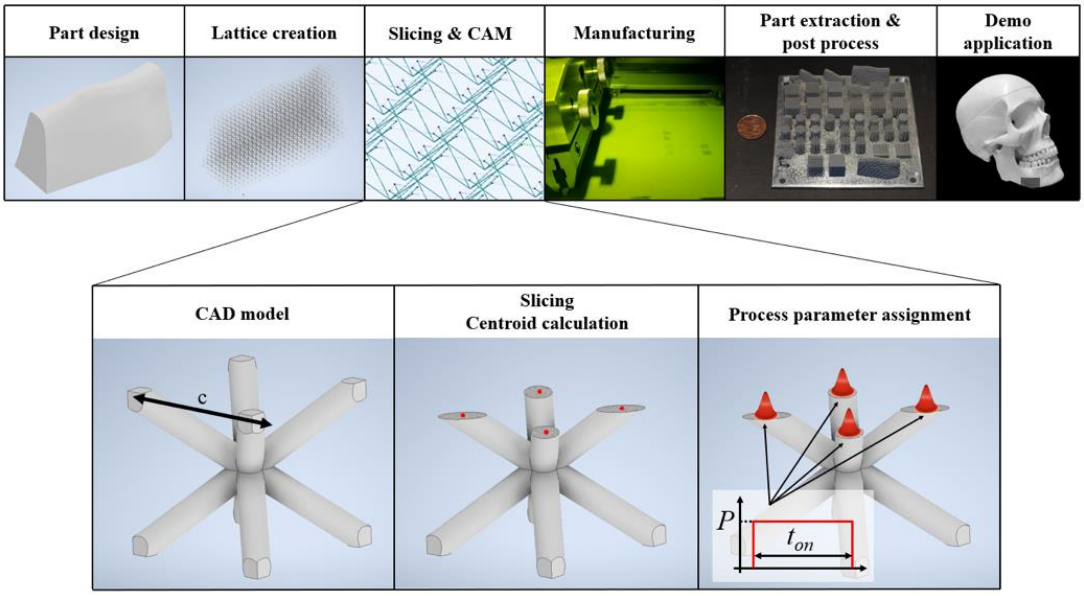


**Figure 2.** Centroid-defined single point exposure applied to the manufacturing of a porous bone scaffold with BCC lattice unitary cell ($c$ is the unitary cell dimension).

# 3 Materials and methods

## 3.1 Materials

A Zn-0.5Mg alloy powder was used in the study. The powder was gas-atomized with spherical form and a size distribution between 15-53 μm (Linbraze, Sommatino, Italy). Figure 3.a shows the powder morphology acquired by SEM. Figure 3.b shows the metallographic cross sections of the powder particles showing full density of the as-provided material, while Figure 3.c shows the powder size distribution. Overall, the powder feedstock matches the requirements of the LPBF application in terms of shape and size.

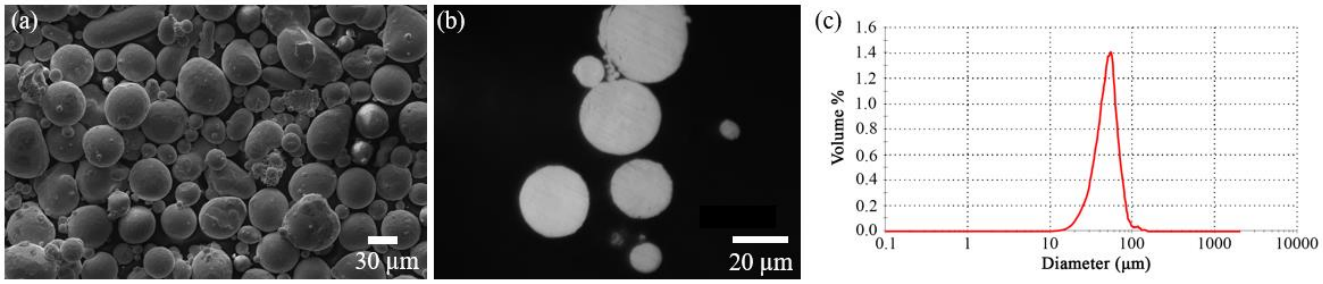


**Figure 3.** (a) SEM image of the powder, (b) metallographic cross section of the particles and (c) PSD estimated using the Circular Equivalent Diameter volume distribution

Table 1 shows the chemical composition of the powder as declared by the producer and as measured through Energy Dispersive X-ray Spectrometry (EDS). The printing substrate was Zn-plated carbon steel plates with a coating thickness of about 300 µm (Sessa snc, Settimo Milanese, Italy). The substrate was roughened by means of 800 grit abrasive paper prior to the LPBF process.

**Table 1.** Chemical composition analysis results by the powder supplier and by EDS measurements

| Measurement | Zn | Mg | Al | O |
|---|---|---|---|---|
| Declared average wt% | 99.47 | 0.52 | 0.005 | nd |
| Declared tolerance wt% | 99.30-99.70 | 0.30-0.70 | <0.010% | nd |
| EDS wt% | 97.9±0.2 | 1.0±0.1 | nd | 1.1±0.1 |

## 3.2 Open industrial LPBF system

An open industrial grade LPBF system, namely 3DNT LLA150R (3DNT, Solbiate Olona, Italy) was employed. The hardware components (laser source and optical chain) and the control architecture were open to the end-user. Customized CAM software able to manage flexible scan strategies including Single Point Exposure was adapted to the LPBF machine (Direct Machining Control, Vilnius, Lithuania). The controller card (SP-ICE3, Raylase, Weßling, Germany) provided the interface between the software and the scanner head (Raylase MS-III). A single mode fiber laser source with 250 W maximum power was employed (MFSC-300L, MAX Photonics, Shezen, China) and 20 µm core fiber diameter. The optical chain was composed by a collimator, a 1.25X beam expander which also provides fine-focus adjustment, the scan head, and an f-theta lens which combined results in a theoretical beam waist diameter ($d_0$) of 27 µm. The main specifications of the system are reported in Table 2.

**Table 2.** Main specification of the LPBF system employed

| Specification | Value |
|---|---|
| Atmosphere | $Ar/N_2$ |
| Maximum emission power, $P_{max}$ (W) | 250 |
| Laser emission wavelength, $\lambda$ (mm) | 1080 |
| Delivery fiber diameter, $d_f$ (µm) | 20 |
| Beam quality factor, $M^2$ | 1.1 |
| Minimum beam diameter, $d_0$ (µm) | 27 |

## 3.3 Experimental Design

Prior to the production of the specimens, laser emission profiles were acquired to reveal the differences between the commanded and emitted pulse durations. The temporal modulation of the laser source has been characterized through a FGA10 InGaAs photodiode (Thorlabs, Newton, NJ, USA) amplified with an operation amplifier (TL072C, Texas Instruments, Dallas, TX, USA). The pulse rise time was considered from the start of the modulation signal to 90% of the maximum power. The pulse fall time was considered from 90% to 10% of the maximum power. The pulse duration ($t_{on,meas}$) was determined as the temporal distance between the initial and final passages from the 10% of the maximum power.

Later, BCC lattice structures with two different levels of unitary lattice cell dimension ($c$=1 and c=2 mm) were manufactured under Ar atmosphere with and $O_2$ content of less than 3000 ppm. Two different macro-geometries of the lattice structures were produced: cubical samples (10 mm x 10 mm x 10 mm, three replicates) and cylindrical samples (Ø 6.5 mm x10 mm, two replicates), designed to optimize micro-CT acquisitions. Both the geometries were manufactured with 2 mm vertical supports, obtained with the same process parameters as the samples. Figure 4 shows the CAD files used for each sample. The layer thickness ($z$) was maintained fixed respectively at a value of $z$=30 µm. The variable parameters, in addition to the cell dimension, were represented by the laser emission power, investigated on two different levels ($P$=40 and 65 W), and by the exposure time, varied on three levels ($t_{on}$=200-400-800 µs). This parameter range was obtained as a result of a preliminary campaign on vertical single struts. Table 3 provides and overview of the fixed and variable process parameters in the present experimental plan.

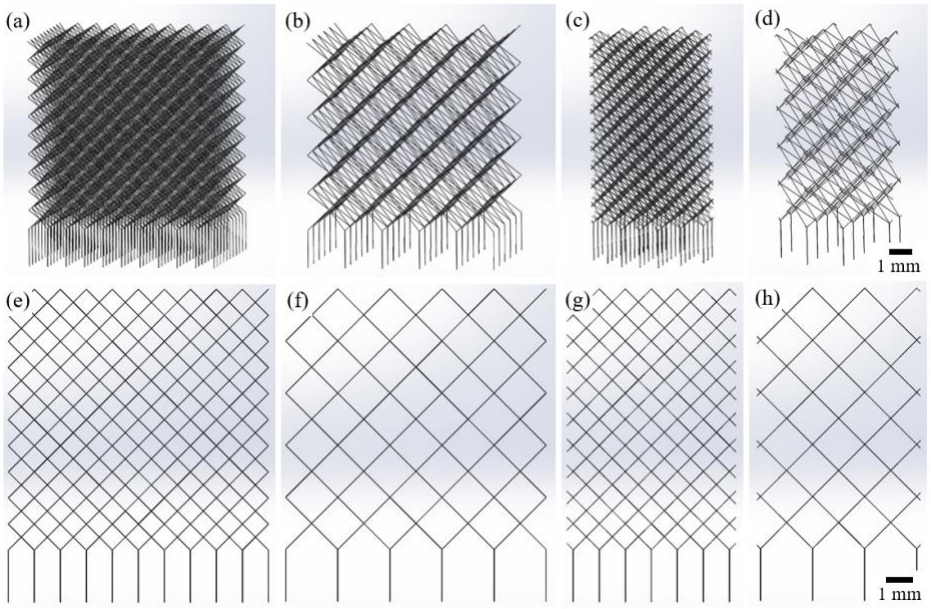


**Figure 4.** CAD models of the BCC lattices with tilted and frontal views: (a) and (e) cubical with $c$=1 mm, (b) and (f) cubical with $c$=2 mm, (c) and (g) cylindrical with $c$=1 mm, and (d) and (h) cylindrical with $c$=2 mm

The cubical samples were qualitatively characterized my means of SEM imaging and subsequently compression testing was performed on all the replicates. Instead, on the cylindrical samples, micro-CT acquisition were performed as well as metallographic cross sectional analyses. An overview of the fixed and variable factors of the experimental campaign is provided in Table 3.

**Table 3.** Fixed and variable factors of experimental campaign

| **Fixed factors** | **Value** |
|---|---|
| Layer thickness, $z$ (μm) | 30 |
| Process gas | Ar |
| Cell type | BCC |
| Beam diameter, $d_0$ (μm) | 27 |
| **Variable factors** | **Value** |
| Cell dimension, $c$ (mm) | 1-2 |
| Laser emission power, $P$ (W) | 40-65 |
| Exposure time, $t_{on}$ (μm) | 200-400-800 |

A craniofacial implant mock-up was also produced as a demonstration of a possible workflow for the production of patient specific bone scaffolds through LPBF exploiting the advantages of SPE scan strategy. The part was

designed as described in 2. A free-form shape filled with BCC lattice structure with $c$=1 mm has been chosen and manufactured, applying the SPE scan strategy with stable process parameters ($P$=65W and $t_{on}$=400 µs).

### 3.4 Characterization

Scanning Electron Microscope (Zeiss EVO 50, Zeiss, Oberkochen, Germany) imaging was carried out for a qualitative analysis by capturing top and side views at different magnifications of the as-built specimens.

Two replicates of the cubical samples were weighted using a digital scale with a resolution of 0.001 g (Precisa 100A-300M). The weight measurement was used to estimate the relative density of the samples as defined as in Equation (1), where $m_0$ is the weight of the fully dense bulk material filling the whole lattice envelope and $m_s$ is the weight of the lattice sample.

$$\rho_{rel} = \frac{m_s}{m_0} \tag{1}$$

Micro computed tomography (CT) images of the cylindrical samples were made (X25 Micro CT scanner, North Star Imaging, Rogers, MN, USA) using a 5 µm voxel size, 140 kV of voltage and 35 µA of intensity. The obtained tomographies were analysed using VGSTUDIO MAX software (Volume Graphics GmbH, Heidelberg, Germany) in order to measure the diameter of the single struts by employing an automated fitting function. Five measurement of random selected single struts were performed for each combination of the process parameters. Tomography images were also exploited to investigate possible formation defects such as porosity through the analysis of the cross sections. Samples were mounted in resin, grinded, polished and the resulting metallographic cross sections were acquired via optical microscopy (UM 300I BD, EchoLab, Paderno Dugnano, Italy) in order to check for the presence of processing porosity. Samples were chemically etched in a 5% HCl and 95% ethanol solution for 20 s in order reveal the microstructure. Figure 5 represents an overview of the characterization methods.

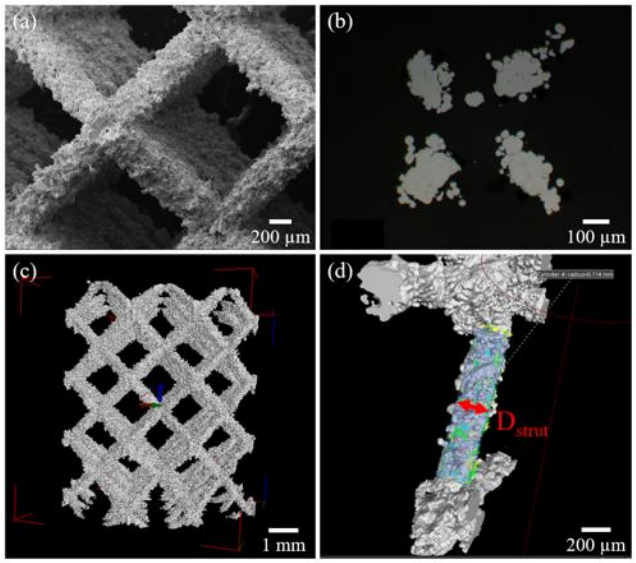


**Figure 5.** (a) Top view SEM image, (b) metallographic cross section of a sample, (c) micro-CT acquisition and (d) strut diameter measurement.

Energy Dispersive X-ray Spectrometry (EDS) was performed on the metallographic cross sections to obtain the chemical composition of the manufactured samples and compare it with the powder one. Four replicates for each processing condition were made. Compression tests were performed on the three replicates of the cubical samples with $c$=1 mm using an MTS Alliance RF/150 electromechanical testing machine (MTS Systems Corporation, Eden Prairie, MN, USA) with a testing range of ±150 kN and 1 N resolution. The tests were performed imposing a 20% maximum strain and a crosshead speed of 2 mm/min. Some preliminary compression tests excluded the lattice structures with $c$=2 mm due to the very low compressive strength (<1 MPa). The condition $c$=1 mm, $P$=40 W and $t_{on}$=200 µs was excluded from the testing due to uncomplete build on the support side. The load vs displacement curves were acquired for all the remaining samples and elaborated using MATLAB (MathWorks, Natick, MA, USA). Representative fracture surfaces of some selected samples have been observed by means of SEM in order to provide a greater understanding of the failure mechanism.

# 4 Results and discussion

## 4.1 Laser emission

Figure 6.a-c shows the pulse profiles as a function of the laser power and pulse duration. It can be seen that the laser source has an initial ramp stabilizing towards the nominal power and a final ramp after the end of the

command signal. Such delays are attributed to the latency of the pump diodes to reach the desired power level [32][33]. Figure 6.d shows in greater detail the rise and fall time and the measured pulse duration definitions. Figure 6.e shows the measured rise and fall times, which are considerably long and were found to be independent of the commanded pulse durations in the tested range.  acquired conditions and the delays characterization.is almost constant for all the power levels. Figure 6.f shows the measured pulse duration ($t_{on,meas}$) against the commanded one ($t_{on}$). The pulses were found to be approximately 73.5 µs longer than the commanded duration a mainly due to the long fall times, while remaining independent from the laser power.

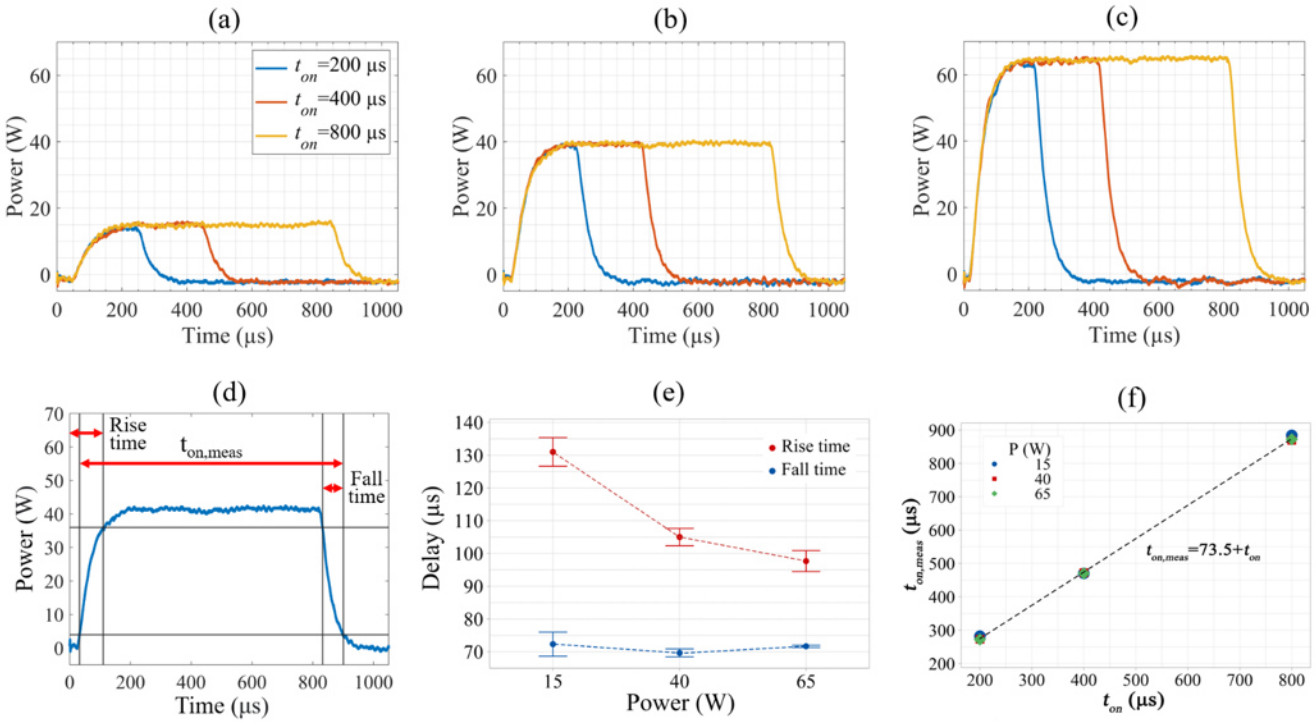


**Figure 6.** Photodiode acquisitions for (a) P=15 W, (b) P=40 W, and (c) P=65 W. (d) Measurements carried out on a signal. (e) The measured rise and (e) fall times against the power levels. (f) Measured pulse duration against the commanded $t_{on}$.

## 4.2 Characterization of lattice structures

During the build process, almost no vapour formation could be detected while spark formation was completely absent, proving the beneficial effect of SPE strategy on the process stability (see the supplementary materials section 6). Indeed, even with a conventional recirculation system, the printing process could be completed without

an accumulation of smoke in the build chamber. As seen in Figure 7, the build process could be completed without macro printing defects. After the removal from the baseplate, partial disintegration was observed on the samples produced using $c$=2 mm, $P$=40 W and $t_{on}$=200 µs. Indeed, this condition is the least energetic amongst the tested with the struts being farther apart from each other. These results confirms the feasibility of SPE for inclined struts (even with overhang angles of around 45°) and complex lattice structures.

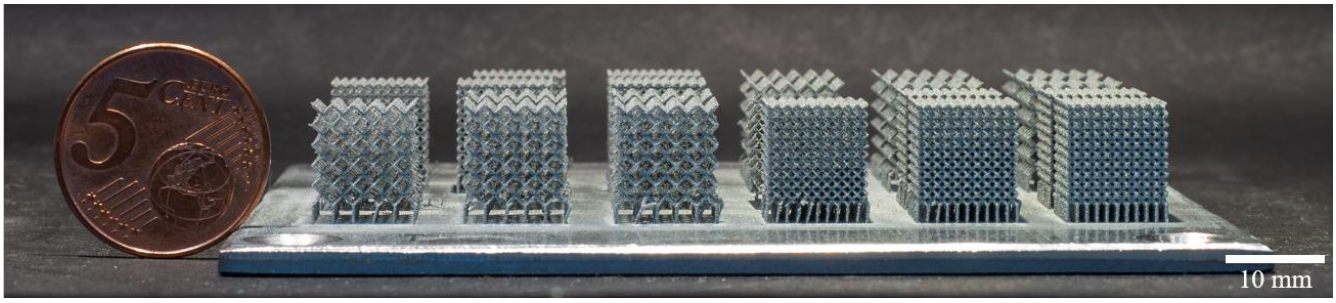


**Figure 7.** Macro images of the cubical samples attached to the build plate

### 4.2.1 SEM imaging

SEM images of the specimens produced with different process parameters are shown in Figure 8. The images show that material consolidation and geometrical accuracy were achieved, despite the presence of sintered powder particles around the struts. The amount of attached particles was not found to be influenced by the process parameters. Instead, the diameter of the single struts seems influenced by the process parameters, increasing both when emission power and exposure time are incremented. From the top view, superficial pores can be seen with the highest energetical input. The probable explanation to the phenomena is the highest thermal accumulation near the strut junctions caused by close sequential single pulse exposures of the powder bed and possible keyhole formation [13].

### 4.2.2 Dimensional characterisation by micro-CT

Figure 8 shows the result of the strut diameter ($D_{strut}$) measurements. The diameter shows an increasing trend with increasing exposure time and power. The numerical results indicate that the SPE scan strategy is able to reduce the smallest feature size and improve the process resolution with respect to conventional vector-based scan strategies. Average strut diameter ranges between 130-350 µm varying the process parameters. An increase in the

power and pulse duration provide increased strut diameter as directly related to the quantity of the released laser energy. The influence of the cell size Therefore with the fixed cell design the enlargement of the struts correspond to the reduction of the pore size. Consequently, it can be deduced that the SPE can allow higher flexibility in controlling strut and pore dimensions in LPBF

Considering spherical powder grains with an average diameter ($D_{avg,particle}$) of 35 µm, cylindrical struts and a layer thickness of 30 µm the average number powder grains melted in the process ($N_{avg}$) could be estimated from the following expression:

$$N_{avg} = \frac{\left(\frac{D_{srut}}{2}\right)^2 \cdot z \cdot \pi}{\left(\frac{D_{avg,particle}}{2}\right)^3 \cdot \frac{4}{3}\pi} \quad (2)$$

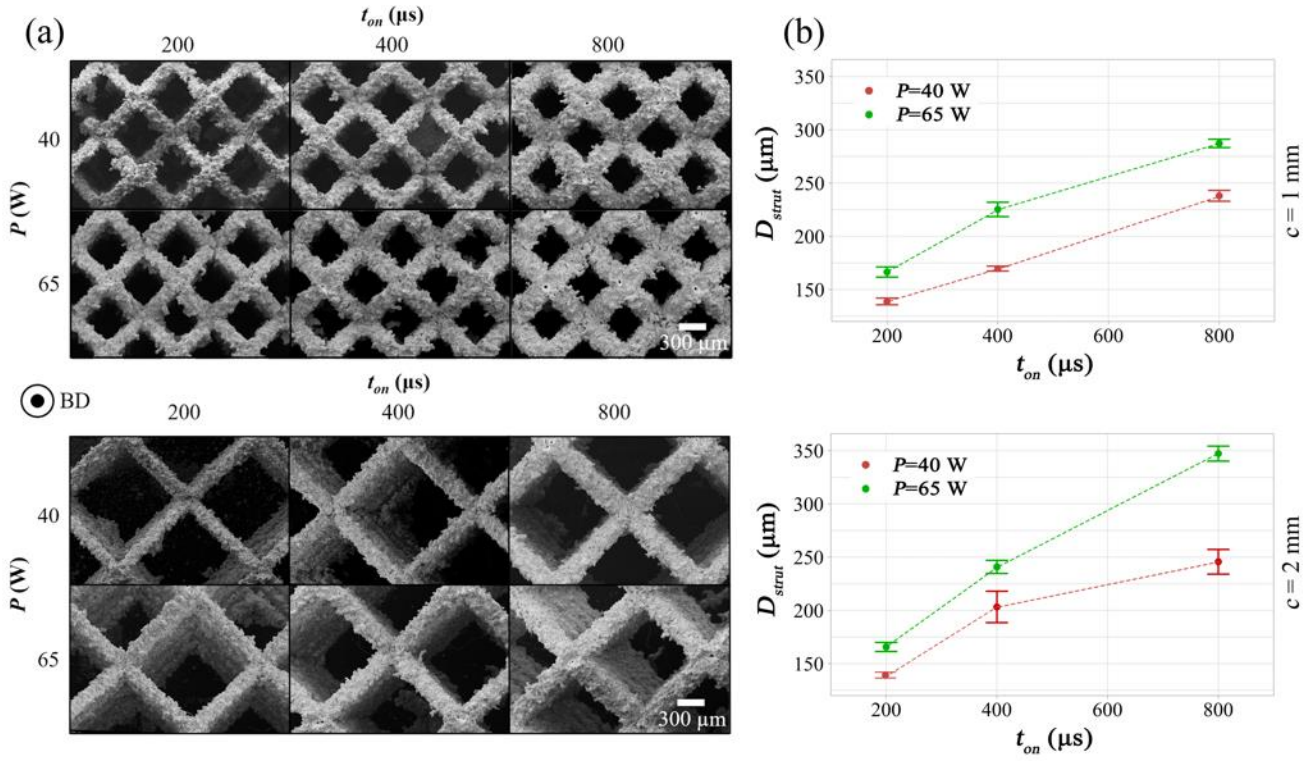


**Figure 8.** (a) SEM top images of a representative condition for each combination of the process parameters and (b) results of the dimensional characterization of the strut diameter. Dashed line depict trend, while the error bars show standard deviation. (BD: build direction)

Accordingly, the process is expected to involve approximately 20 to 130 powder grains in average per strut at each layer depending on the process parameters. It can be concluded that beyond the advantages provided to reduce the vapour formation and improve the process stability, PSE appears to improve the process resolution to an extent of a few grains with respect to conventional vector-based scan strategies. Indeed, comparing the result with the previous works involving the LPBF production of Zn alloy lattice samples [15,18,34,35], the values obtained in the present investigation are significantly lower. A finer resolution of the process is beneficial for biomedical applications since it allows the creation of features with a specific microgeometry, customization of the size and shape of the pores could be possible with a greater accuracy. Moreover, considering the requirement for bone scaffolds regarding pore size (i.e. 300-900 μm [5]), the strut dimensions with $c$=1 mm cell size could be flexibly varied by adjusting the process parameters.

#### 4.2.3 Internal defects and relative density

Figure 9 shows cross-sections of the samples as a function of the process parameters. The images showed full melting and consolidation of the material in the central part of the strut, with sintered and loosely adhered powder particles around the fused zones of the strut borders as no post processing was applied to improve the surface quality. The amount of the sintered particles depended on the processing parameters, where with more energetic conditions the fraction of melted region compared to the sintered particles appears to be higher. Generally, no macro pores were identified from the image analysis and the density seems constant varying the process parameters. The pore formation was observed to occur occasionally in the strut junctions, presumably due to the thermal build up effect created by four subsequent and spatially close laser exposures.

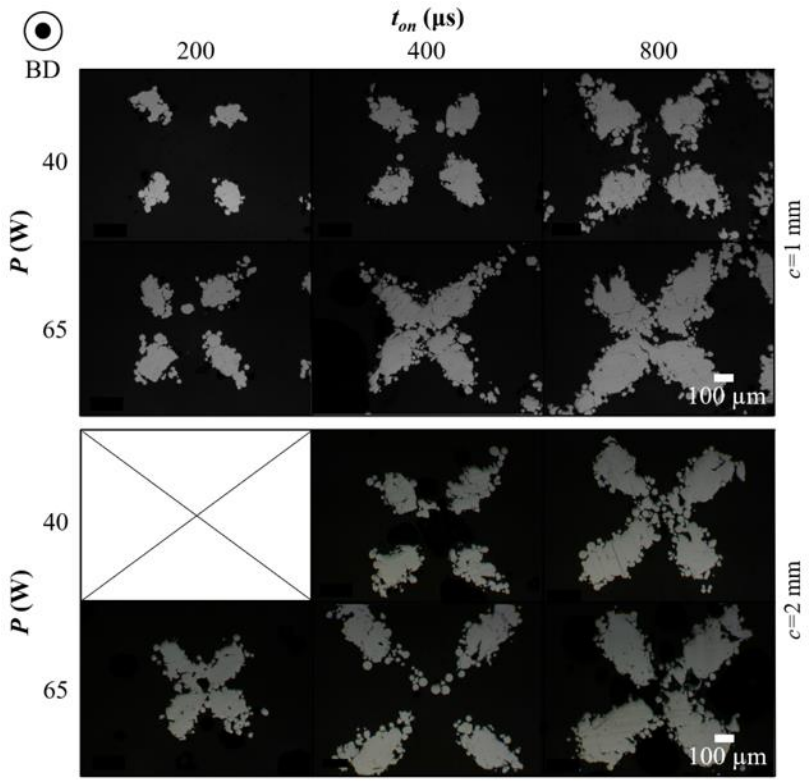


**Figure 9.** Metallographic cross-sections acquired through optical microscopy of a representative condition for each combination of the process parameters (BD: build direction).

Figure 10 reports the relative density ($\rho_{rel}$) values obtained. The values show an increasing trend both with exposure time and power increment. The relative density trend is analogous to the variations of strut diameter as could be expected. Average relative densities varied in the 6.5-34.2 % range for $c$=1 mm and in the 1.7-10.4 % range for $c$=2 mm.

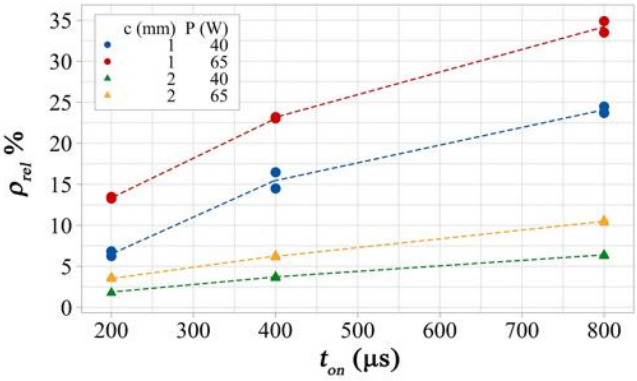


**Figure 10.** Results of the relative density measurements (dashed lines depict trend).

### 4.2.4 Chemical composition

The results from the EDS analysis are shown in Figure 11. It should be noted that the analysed material depth is approximately 3 µm, and the measurements remain of qualitative nature. Overall, the EDS measurements slightly vary compared to the declared values by the powder producer mainly due to the presence of oxygen. The relatively higher oxygen content can be related to the low penetration depth of EDS and the difficulty of measuring lighter elements via EDS. The relatively higher level of oxygen appears to decrease the Zn content with respect to the declared value of the powder feedstock, while the Mg contents seem to slightly higher than the declared ones. Hence, the measurements especially concerning the oxygen content via EDS is indicative should be compared with the EDS measurements of the powder feedstock. From the qualitative perspective, the LPBF processed lattices appear to be more oxidised compared to the powder feedstock, which results in a slight reduction of Zn. Although qualitative, similar oxygen contents have been reported during the LPBF of pure Zn [14][18]. The oxygen content in the process atmosphere (3000 ppm) may have induced the increase in the oxide content. The Mg content appears to remain almost unvaried overall compared to the feedstock. It can be expected that Zn having a lower vaporization point ($T_v$=1180 K) compare to Mg ($T_v$=1363 K), and therefore it is depleted more easily [36]. Overall, it can be concluded that PSE provides a further advantage of not altering the chemical composition of the processed Zn-Mg alloy thanks to the controlled energy release on the material.

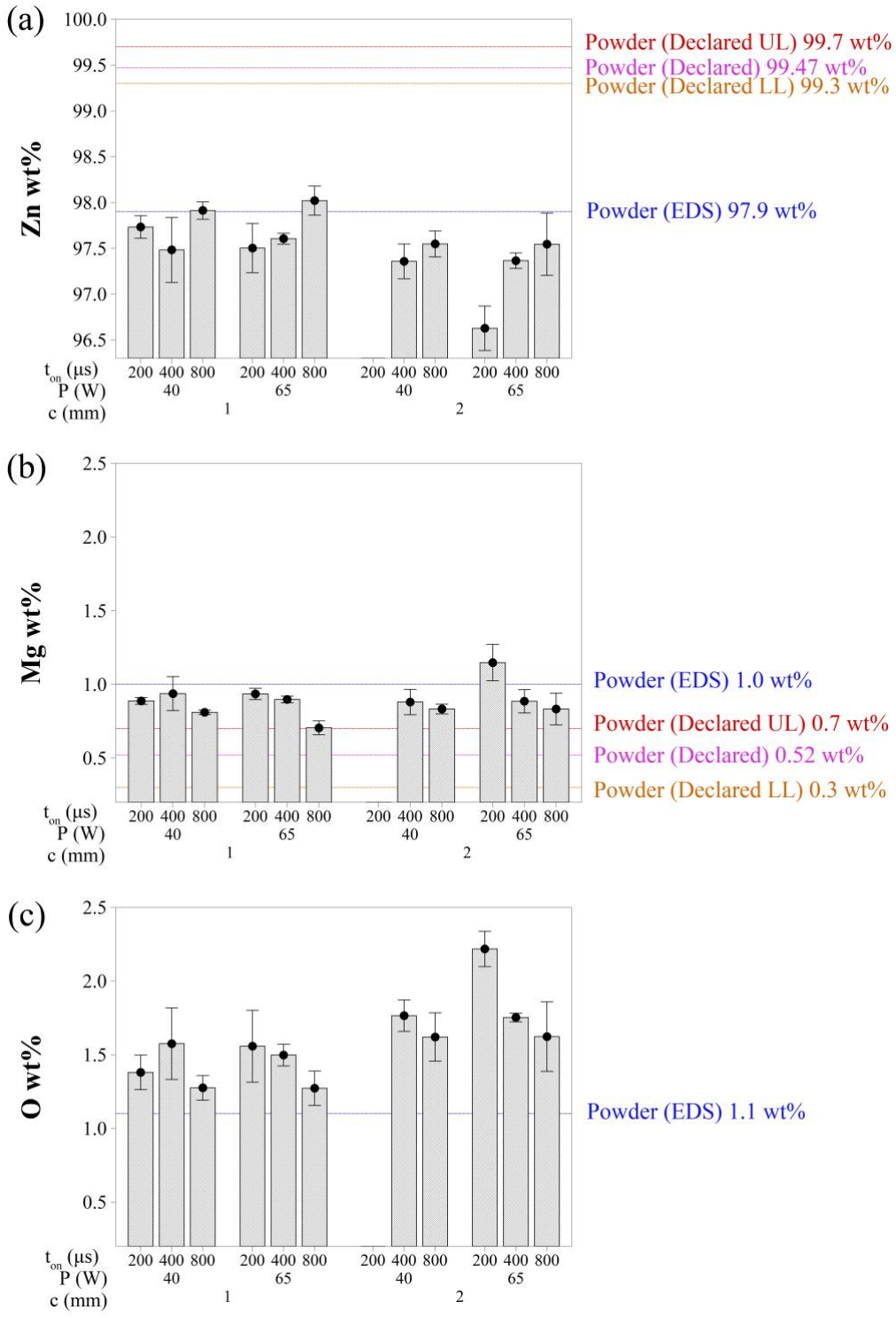


**Figure 11.** Results from the EDS measurements performed on the lattice samples, compared with reference EDS measurements on powder and with the declared powder composition as provided by the supplier. Error bars show standard deviation. (UL=Upper Limit, LL=Lower Limit)

### 4.2.5 Microstructure

Figure 12 shows the microstructure of the lattice produced with $P$=40W, $t$=800 µs, $c$=2 mm. The microstructure is uniform and shows no preferential orientation over the exposed region. The microstructure confirms full consolidation at each single strut. By comparing the microstructure obtained in the present research with as-cast samples of the same alloy [37] [38], a significantly refined grain size (4.8±1.7 µm) can be noted in the LPBF samples processed with SPE strategy. The grains are surrounded by a network-like structure expected to be $Mg_2Zn_{11}$ and produced by the rapid cooling during the process [37]. By comparing the microstructure obtained in the present research with as-extruded samples of the same alloy at 200°C and 300°C [39], a refined grain size can still be noted, while the preferential grain orientation visible in the extruded samples is absent in the LPBF ones. The homogenous and fine can be beneficial for controlling the degradation behaviour as well as the mechanical properties [10]. A more detailed analysis of the microstructural evolution, which was not along the main aims of the present work, should provide further comprehension to the use of the alloy in the final application [40].

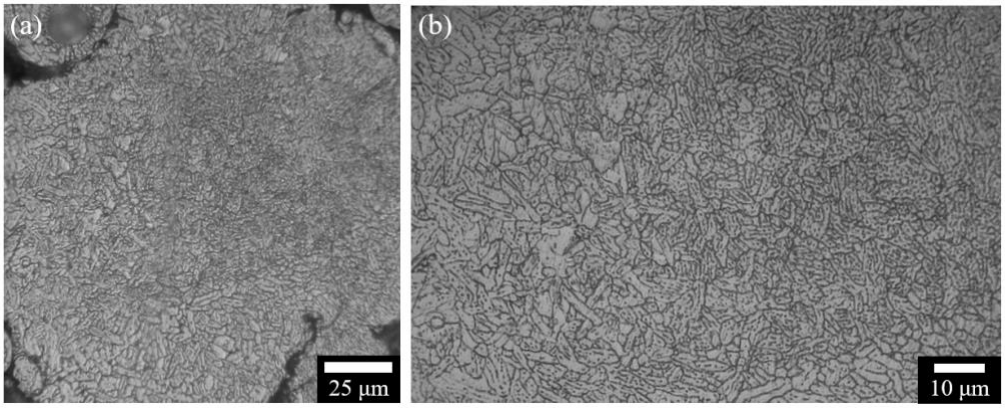


**Figure 12.** Typical microstructure of Zn-0.5Mg lattice taken at the scan plane at low magnification (a) and high magnification (b)

### 4.2.6 Mechanical behaviour

Figure 13 shows the stress ($\sigma$) - strain ($\varepsilon$) curves acquired of struts with $c$=1 mm. The graph shows a marked influence of the process parameters, both exposure time and power, on the resulting properties of the lattice.

Generally, the curves show an initial elastic portion, then a plastic deformation section followed by a drop in the stress value, corresponding to the breakage of the sample.

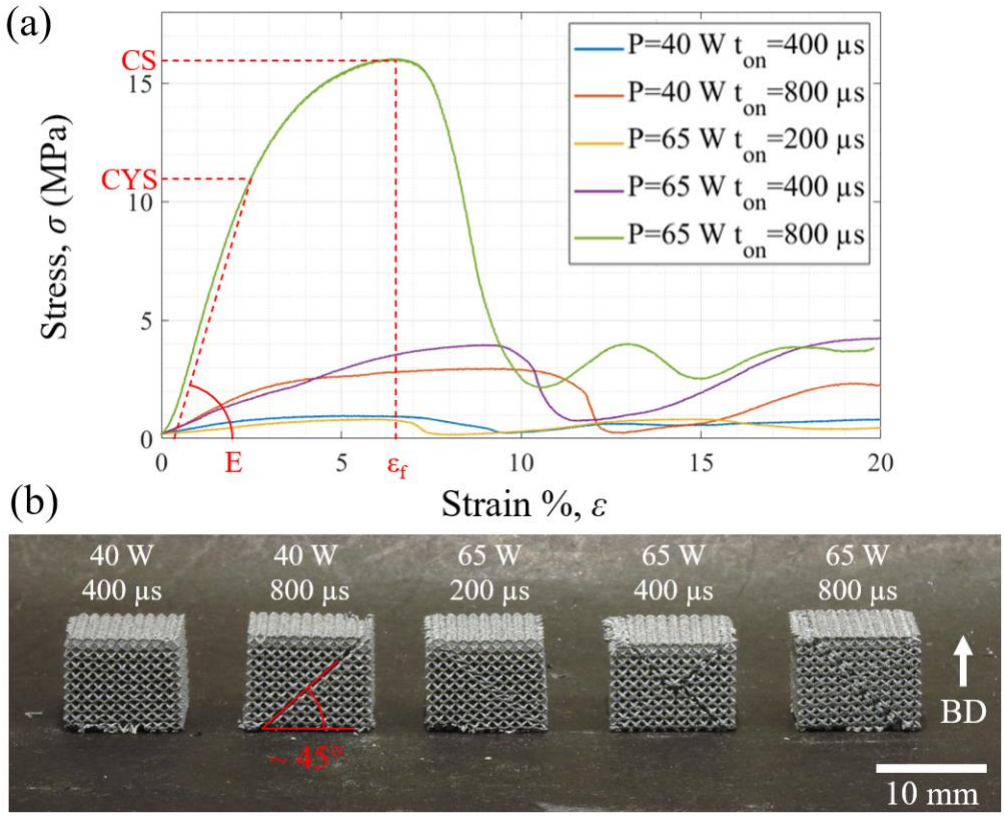


**Figure 13.** (a) Stress ($\sigma$) - strain ($\varepsilon$) curves of the produced lattices with $c$=1 mm. (b) Macro images of the samples after compression testing.

As shown in Figure 13, in most of the cases the fracture surface was angled at 45° with respect to the load direction. Such behaviour has been observed in literature for stretch-dominated lattice structures [41], while theoretically the BCC lattice employed in the present investigation is regarded as a bending-dominated structure.

Compressive Yield Strength (*CYS*), Compressive Strength (*CS*), Young's Modulus (*E*) and Strain at failure ($\varepsilon_f$) were extracted from the stress-strain curves. An overview of the mechanical properties obtained for $c$=1 mm are reported in Figure 14. The compressive yield strength, compressive strength and Young's modulus show a similar trend, increasing both with exposure time and power increment. The value of the strain at failure instead seems rather constant regardless of the process parameters used. The sample with the highest mechanical properties ($c$=1

mm, $P$=65 W and $t_{on}$=800 µs) showed a CS of 14.7±0.7 MPa, a CYS of 10.8±1 MPa, a Young's Modulus of 358±110 MPa and a strain at failure of 8.8±2.0 %.

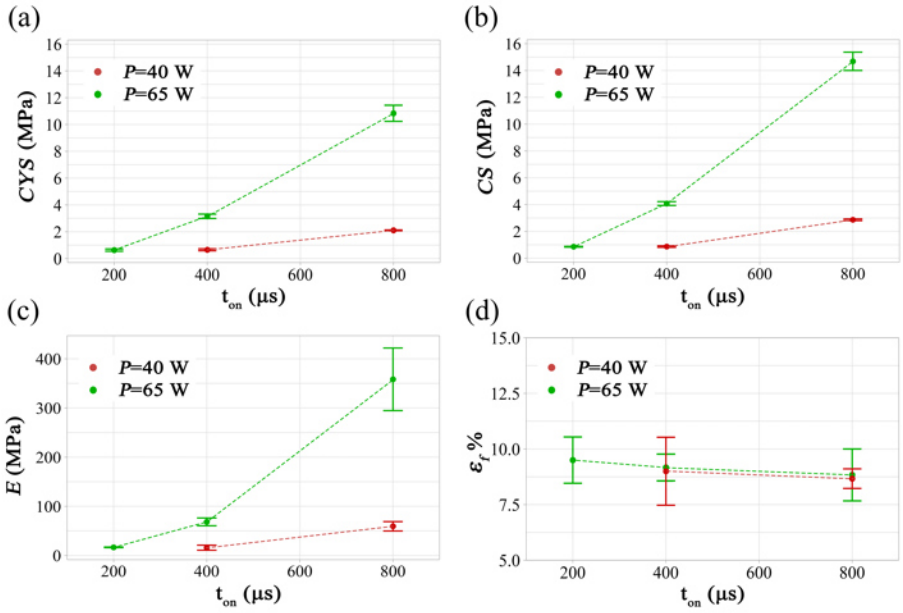


**Figure 14.** Overview of the mechanical properties obtained for lattices with $c$=1 mm, (a) compressive yield strength, (b) compressive strength, (c) Young's modulus, (d) strain at failure. Dashed line depict trend, while the error bars show standard deviation.

Fracture surfaces were observed by means of SEM microscopy in order to understand the failure mode of the structures, a representative case of the acquired images can be seen in Figure 15. The fracture locations can be identified as the brighter areas in (a), it can be noticed that the failure of the single struts mostly happened near the junction. By increasing the magnification of the fracture surface (c), the typical aspect of transgranular fractures can be recognized, indicating that on a microscale a fragile fracture occurred [42]. The absence of plasticization areas support such observation. The location of the fracture surfaces can be explained considering that under compression BCC lattice structures show a stress concentration in that area [43]. Furthermore, some build defects (localized porosity) were occasionally present in such position and could have aided the local failure of the structure. The fragility observed both through micro and macro analysis of fractured specimen may be caused by the local stress concentration (due to the geometry or the presence of localised defects) or may also be correlated to the intrinsic behaviour of the material (also considering the fabrication method which relies on a fast melting and rapid solidification process). Previous works on Zn-xMg alloys processed by LPBF highlighted a sharp

decrease in the ductility of the material with an increasing Mg content [44]. The observed fracture behaviour is expected to be a result of the combination of these effects. Overall, the fracture surfaces show that the lattices broke in the fully melted region, indicating that the sintered particles remained around the borders. In order to increase the mechanical properties, further improvement of the process parameters to reduce the sintered material amount as well as post processing strategies can be applied [45][46].

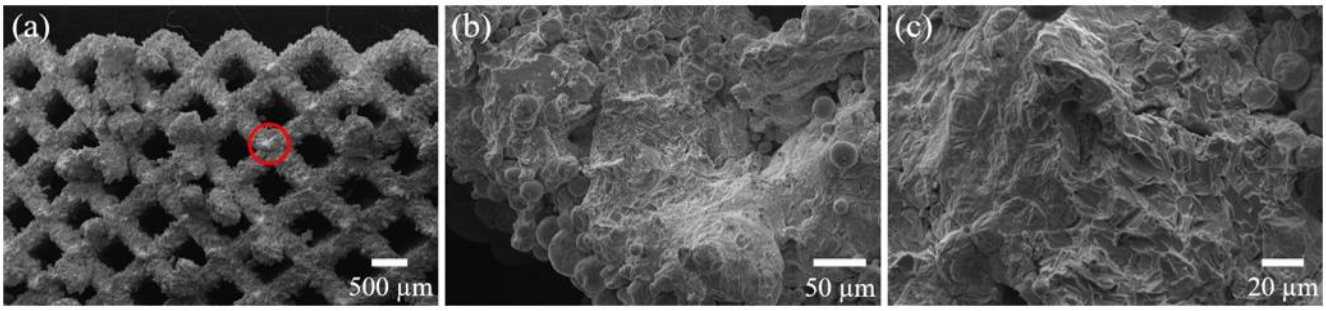


**Figure 15.** SEM images of the fracture surfaces: (a) showing fracture locations, (b) higher magnification on the detail highlighted in the previous image and (c) high magnification image showing transgranular brittle fracture

Due to the nature of the proposed application of the lattice structures, i.e. bone scaffolds, the mechanical properties represent a crucial point and their dependence upon the structure geometry should be considered. Relative strength ($\frac{\sigma^*}{\sigma_{y,s}}$) and relative elastic modulus dependence upon the relative density has been modelled by Gibson [47] and Ashby [48] for open cell solids as a positive exponent relationship. This approach has been confirmed for LPBF lattice structures [49] and can be expressed as in Equation (3)

$$\frac{\sigma^*}{\sigma_{y,s}} = C\left(\frac{\rho^*}{\rho_s}\right)^n \tag{3}$$

where $\sigma^*$ is the static yield strength of the lattice structures, $\sigma_{y,s}$ is the static yield strength of the lattice structure's bulk material, $C$ is the Gibson-Ashby constant, the value of which is dependent on the unit cell topology and $n$ is the exponent, where $C$ and $n$ are experimentally determined and depend on the material and the geometry of the lattice structure unitary cell [48],[49].

The experimental coefficients of the Gibson-Ashby model were calculated via non-linear regression fitting and using the experimental compression yield strength (*CYS*) and relative density ($\rho_{rel}=\frac{\rho^*}{\rho_s}$) data. Literature data was used for the bulk material properties ($\sigma_{y,s}$=230 MPa [44]). A single fitting was initially performed for lattices produces with the two levels of the laser emission power, which resulted in lack-of-fit. This indicates that the model does not fit the data well, indicating that the model may be missing further predictors [50]. As a next step, the data points of the different power levels were separated to fit separate models. In this case no lack-of-fit was observed. The fitted curves for the are shown in Figure 16 along with the calculated coefficients along and their 95% confidence intervals for the mean. Although the limited number of specimens, the fitted models appear to follow the data points well. The results indicate that the *C* parameter is largely different between the two levels of laser emission power, suggesting that the LPBF material properties are influenced by the power level. According to the Gibson-Ashby model, the metallic lattices should have the *C* coefficient between 0.1 and 1 [49]. The struts produced with 40 W laser power fall within this range, while the ones produced with 65 W appear to have the *C* value much higher presumably showing increased strength independently from the lattice geometry. Considering the sensitivity of the material to the temperature, such phenomenon is likely to occur as a function of the process parameters changing the mechanical behaviour. On the other hand, the exponent *n* appears to remain in a similar range for the two power levels, the confidence intervals including the value of 3 in both cases. Indeed, for BCC lattice structures the common value for *n* parameter is about 1.5, while bend-dominated lattice walls and struts can reach $n\approx$2-3 [51]. Moreover, the higher exponent values trend found in this work can be caused by a modification of the mechanical properties of the material with increasing exposure time, leading to an effect superimposed to the pure geometrical effect of the relative density.

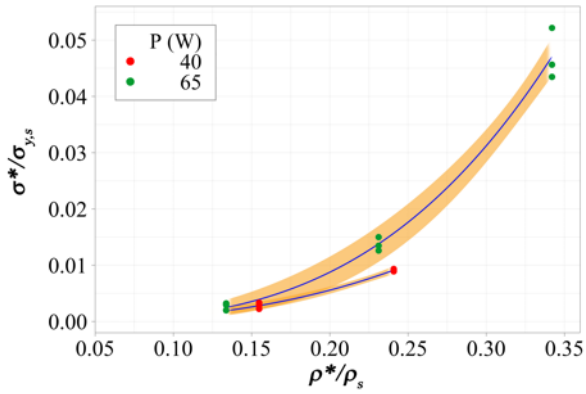


| Coefficient | *P*=40W (95% CI) | *P*=60W (95% CI) |
|---|---|---|
| *C* | 0.39 (0.19; 0.99) | 1.35 (0.73; 2.95) |
| *n* | 2.7 (2.1; 3.3) | 3.1 (2.6; 3.8) |

**Figure 16.** $\frac{\sigma^*}{\sigma_{y,s}}$ as a function of $\frac{\rho^*}{\rho_s}$ with the fitted Gibbs-Ashby model. The shaded regions represent the 95% confidence intervals for the fits. The regression coefficients are given separately for the two different power levels with their 95% confidence intervals.

**Table 4.** Overview of the literature results compared with the ones of the present research and with the reference values for bone scaffolds (* data are extrapolated from plots)

| Type of lattice | Alloy | Cell size (mm) | $D_{strut}$ (µm) | $\rho_{rel}$ (%) | CS (MPa) | CYS (MPa) | E (MPa) | Strain at failure % | Ref. |
|---|---|---|---|---|---|---|---|---|---|
| BCC | Zn-0.5Mg | 1 | 287±9 | 34 | 14.7±0.7 | 10.8±1.0 | 358±110 | 8.8±2.0 | Present work |
| Diamond | Pure Zn | 1.4 | 441±1 | 38±2 | 15* | 10.8±0.2* | 786±80* | - | [34] |
| Diamond | Pure Zn | 1.4* | 562 | 55±1.8 | 22.9 ±1.7 | 12.7± 1.5 | 950±114 | - | [35] |
| Diamond | Zn-2WE43 | 1.4* | 562 | 55±1.8 | 60.5 ±1.1 | 50.9± 1.0 | 1910±257 | - | [35] |
| Diamond | Zn-5WE43 | 1.4* | 562 | 55±1.8 | 73.2 ±2.6 | 66.2± 2.4 | 2480±270 | - | [35] |
| Diamond | Zn-8WE43 | 1.4* | 562 | 55±1.8 | 50.9 ±3.1 | 50.9± 3.1 | 2540±203 | - | [35] |

| Reference | CS (MPa) | E (MPa) | |
|---|---|---|---|
| Cortical bone | 90-205 | 1000-35000 | [5] |
| Cancellous bone | 0.1-14 | 100-1400 | [5] |

The results of this work can be compared to the other Zn based lattices produced via LPBF in literature. The processing conditions providing the largest struts with *c*=1 mm cell dimension was considered for the comparison (*P*=65 W, $t_{on}$=800 µs). An overview of the results is provided in Table 4 together with the reference values for cortical and cancellous bone. It can be seen that the reference works are very limited, alloy types and lattice geometries vary. Li et al studied diamond lattices with pure Zn [34]. Qin et al studied the LPBF of Zn-xWE alloys

by mixing pure Zn and WE43 Mg alloy [35]. The limited literature reflects the difficulty in developing and comparing new alloys due to the low processability of Zn-alloys, where results are often compared to within the single work. As per the difficulty in comparison, a complete overview with the lattice type, the alloy employed, the cell size and the strut diameter is provided together with the relative density and the mechanical properties. The final mechanical properties rely on the defects, microstructure as well as the strut size and the lattice geometry. From this perspective the normalized compressive yield strength is a parameter that can yield a clearer analysis. The strut sizes of the SPE produced lattices of this work have 25% to 40% of the strut cross-sections of the reported works in the literature along with a lower relative density [34], [35]. The PSE produced Zn-0.5Mg BCC lattices have an intermediate mechanical behaviour between diamond pure Zn and Zn-xWE43 lattices [34] [35]. Overall, the elastic modulus is much smaller resulting in a less rigid behaviour more compatible with cancellous bone. The material strength of PSE produced lattices is much lower than those of Zn-xWE43 alloys due to the geometrical differences as well as the alloying constituents [35]. Combined with the smaller cell size used in the PSE produced Zn-0.5Mg the thinner struts allow reducing pore dimensions further. Such conditions are expected to be favourable for bone growth mimicking the material properties towards the cancellous bone structure [52]. The smaller pores are expected to enhance the wicking behaviour favouring the transport of body fluids and nutrients along the porous material [53]. The geometrical effects are expected to also have an impact on the corrosion behaviour. The smaller struts provide a larger surface area to volume ratio, which can induce a more rapid biodegradation behaviour. If the biodegradation can be followed by further growth of the bone structure, the thinner Zn-alloy struts can provide the means for healing larger fixation regions.

Further increase of the mechanical properties is viable through the modification of the lattice geometry but also addition of the alloying elements. The results highlight that the PSE provides process stability for the given material and the possibility to adjust the strut size by adjusting the process parameters. Further improvement of the mechanical properties can be achieved by geometrical optimization, the use of other lattice types and alloys combined with the use of the PSE strategy.

## 4.3 Implant mock-up

The implant mock-up was produced without excessive smoke or spark generation during the processing. Figure 17 shows the additively manufactured Zn-alloy mock-up implant mounted on a polymeric cranial model. The implant mock-up mimics the conformal bridging of a jaw defect by means of a customized design. For the purpose of the demonstrator, no fixation principles was considered. It can be seen that the geometrical matching of the model scaffold with the bone defect has been maintained. While clinical reality will require much more detailed analysis of the design and implantation phases, the produced mock-up shows the flexibility of using SPE in producing customized biodegradable implants. A video of the LPBF process during the production of the implant mock-up is provided in the supplementary materials.

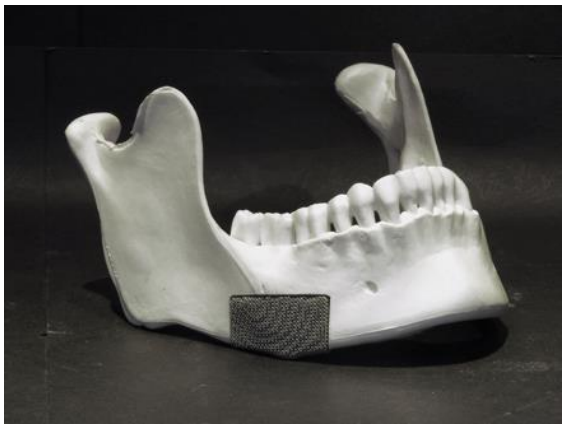

**Figure 17.** Implant mock-up positioned as a filling scaffold for the a jawbone defect.

Overall, the developed PSE strategy is proven to be capable of producing thin biodegradable Zn-0.5Mg struts and lattices, which can be conformally formed around an implant geometry. The process parameters were found to be effective in managing the strut size rather than the use of consecutive scan vectors or exposure points over the scanned geometry. Prior to the final use of the developed components with the combination of the biodegradable alloy and the novel scan strategy extensive analyses on the biodegradation behaviour, and cytocompatibility aspects should be carried out.

The presented PSE approach relies on the modifications of software and laser beam control. The majority of the conventional LPBF systems operate with fiber lasers and scanner optics similar to what has been used in this work.

The type of power modulation is readily available to these lasers along with the controller capabilities of the scanners. Hence, for future implementations retrofitting such scanning solutions to existing machines is a highly feasible option.

# 5 Conclusions

This work demonstrated development and use of single point exposure strategy in LPBF for producing biodegradable Zn-0.5Mg alloy lattice. The work showed the passages from software integration to process development, material analysis to finally a geometrical demonstrator. The main results of the work can be summarized as follows.

- The use of SPE system on an open industrial LPBF system was enabled through software changes rendering such option highly viable for existing machines. The strategy allowed the suppression of smoke and spark formation during the process, avoiding the need of a modification of the recirculation system of the machine.
- The strategy allowed to fully consolidate Zn-0.5Mg BCC lattice structures with strut diameters in the 130-350 μm range, significantly lower than the technological limits currently recorded in literature sources. The cross sectional analysis shows a general full consolidation with a limited amount of localized porosity at the strut junctions. The microstructure was found to be consisted of fine grains homogenously distributed along the strut.
- The failure mode of the lattice structures under compression a 45° fracture plane and a fragile fracture of the single struts. Moreover, the mechanical model employed for the discussion of the results allowed to determine the parameters for the exponential relationship between compressive strength and relative density and highlighted a bending mode with higher exponential trend with respect to literature sources, suggesting an influence of the process parameters superimposed to the pure geometrical effect. These mechanical behaviours do not belong to the stretch-dominated.
- The PSE process parameters varied the mechanical properties of the lattices with the same design. The highest compressive strength was achieved with the most energetic condition at 14.7±0.7 MPa with a strut

size of 287±9 µm and 34% relative density. Such properties are promising to match those of the cancellous bone. The small struts and pores can be advantageous for promoting bone growth and biodegradation control.

- The use of PSE for producing custom biodegradable implants with conformal shape to the bone defect was demonstrated with a mock-up for a bone defect on a model, demonstrating the applicability of SPE to complex freeform geometries..

The present work showed in a systematic way process development and characterization for the biodegradable Zn-alloy. Further development of this work include a more comprehensive mechanical characterization concerning fatigue behaviour as well as residual strength upon biodegradation. The biodegradation rates as well as biocompatibility issues should be investigated. Concerning the use of PSE in LPBF, the processability studies can be extended to conventional LPBF alloys for improved process resolution or to other difficult to process materials such as Mg alloys. Another aspect regards the programming of process parameter allocation for more complex lattices based on strut size variations or surfaces, which can benefit from the use of PSE.

# 6 Appendix

Figure A. 1 shows a frame of the acquired video during the printing of the cubical lattice samples. In the frame, the sample with the highest energy input is being scanned and minimal vaporization with no spark formation.

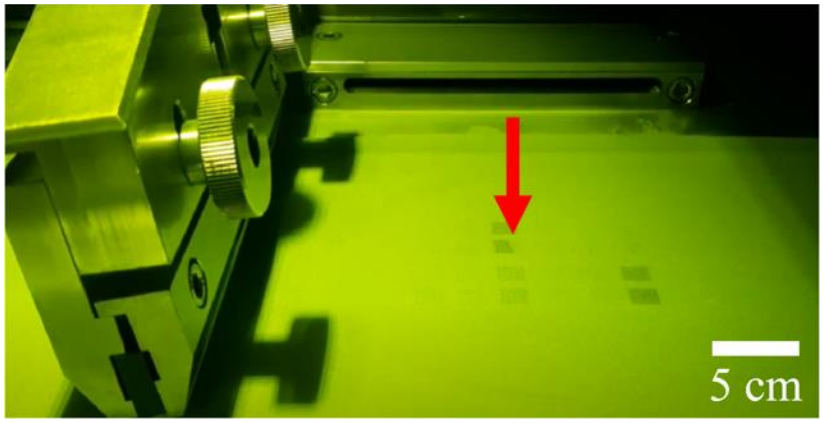


**Figure A. 1.** Single frame from the processing video of the cubical lattice structures

The considerations regarding process stability and suppression of vapour formation are confirmed in Figure A. 2 where a frame from the video acquired during the processing of the implant mock-up can be seen

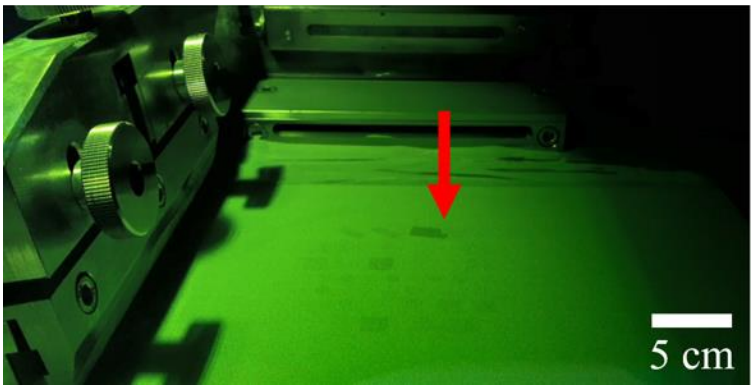


**Figure A. 2.** Single frame from the processing video of the implant mock-up

## Acknowledgements

The Italian Ministry of Education, University and Research is acknowledged for the support provided through the Project "Department of Excellence LIS4.0 - Lightweight and Smart Structures for Industry 4.0". The authors are grateful to Direct Machining Control and Raylase for the technical support provided.

## References

[1] A.A. Zadpoor, Additively manufactured porous metallic biomaterials, J. Mater. Chem. B. 7 (2019) 4088–4117. doi:10.1039/c9tb00420c.

[2] S.J. Hollister, Porous scaffold design for tissue engineering, Nat. Mater. 4 (2005) 518–524.

[3] M. Navarro, A. Michiardi, O. Castano, J.A. Planell, Biomaterials in orthopaedics, J. R. Soc. Interface. 5 (2008) 1137–1158.

[4] C.M. Murphy, M.G. Haugh, F.J. O'brien, The effect of mean pore size on cell attachment, proliferation and migration in collagen–glycosaminoglycan scaffolds for bone tissue engineering, Biomaterials. 31 (2010) 461–466.

[5] D. Carluccio, A.G. Demir, M.J. Bermingham, M.S. Dargusch, Challenges and Opportunities in the

Selective Laser Melting of Biodegradable Metals for Load-Bearing Bone Scaffold Applications, Metall. Mater. Trans. A Phys. Metall. Mater. Sci. (2020). doi:10.1007/s11661-020-05796-z.

[6] L. Roseti, V. Parisi, M. Petretta, C. Cavallo, G. Desando, I. Bartolotti, B. Grigolo, Scaffolds for bone tissue engineering: state of the art and new perspectives, Mater. Sci. Eng. C. 78 (2017) 1246–1262.

[7] Y. Qin, P. Wen, H. Guo, D. Xia, Y. Zheng, L. Jauer, R. Poprawe, M. Voshage, J.H. Schleifenbaum, Additive manufacturing of biodegradable metals: Current research status and future perspectives, Acta Biomater. 98 (2019) 3–22. doi:10.1016/j.actbio.2019.04.046.

[8] P.K. Bowen, J. Drelich, J. Goldman, Zinc exhibits ideal physiological corrosion behavior for bioabsorbable stents, Adv. Mater. 25 (2013) 2577–2582. doi:10.1002/adma.201300226.

[9] H.F. Li, X.H. Xie, Y.F. Zheng, Y. Cong, F.Y. Zhou, K.J. Qiu, X. Wang, S.H. Chen, L. Huang, L. Tian, L. Qin, Development of biodegradable Zn-1X binary alloys with nutrient alloying elements Mg, Ca and Sr, Sci. Rep. 5 (2015) 1–14. doi:10.1038/srep10719.

[10] D. Carluccio, C. Xu, J. Venezuela, Y. Cao, D. Kent, M. Bermingham, A.G. Demir, B. Previtali, Q. Ye, M. Dargusch, Additively manufactured iron-manganese for biodegradable porous load-bearing bone scaffold applications, Acta Biomater. 103 (2020) 346–360. doi:10.1016/j.actbio.2019.12.018.

[11] M. Montani, A.G. Demir, E. Mostaed, M. Vedani, B. Previtali, Processability of pure Zn and pure Fe by SLM for biodegradable metallic implant manufacturing, Rapid Prototyp. J. 23 (2017) 514–523. doi:10.1108/RPJ-08-2015-0100.

[12] M. Grasso, A.G. Demir, B. Previtali, B.M. Colosimo, In situ monitoring of selective laser melting of zinc powder via infrared imaging of the process plume, Robot. Comput. Integr. Manuf. 49 (2018) 229–239. doi:10.1016/j.rcim.2017.07.001.

[13] A.F.H. Kaplan, M. Mizutani, S. Katayama, A. Matsunawa, Unbounded keyhole collapse and bubble

formation during pulsed laser interaction with liquid zinc, J. Phys. D. Appl. Phys. 35 (2002) 1218–1228. doi:10.1088/0022-3727/35/11/319.

[14] A.G. Demir, L. Monguzzi, B. Previtali, Selective laser melting of pure Zn with high density for biodegradable implant manufacturing, Addit. Manuf. 15 (2017) 20–28. doi:10.1016/j.addma.2017.03.004.

[15] P. Wen, M. Voshage, L. Jauer, Y. Chen, Y. Qin, R. Poprawe, J.H. Schleifenbaum, Laser additive manufacturing of Zn metal parts for biodegradable applications: Processing, formation quality and mechanical properties, Mater. Des. 155 (2018) 36–45. doi:10.1016/J.MATDES.2018.05.057.

[16] K. Lietaert, W. Baekelant, L. Thijs, J. Vleugels, Direct metal printing of zinc: From single laser tracks to high density parts, World PM 2016 Congr. Exhib. (2016) 1–6.

[17] Y. Chen, P. Wen, M. Voshage, L. Jauer, Y. Qin, J.H. Schleifenbaum, R. Poprawe, Laser additive manufacturing of Zn metal parts for biodegradable implants: Effect of gas flow on evaporation and formation quality, J. Laser Appl. 31 (2019) 022304. doi:10.2351/1.5096118.

[18] P. Wen, Y. Qin, Y. Chen, M. Voshage, L. Jauer, R. Poprawe, J.H. Schleifenbaum, Laser additive manufacturing of Zn porous scaffolds: Shielding gas flow, surface quality and densification, J. Mater. Sci. Technol. 35 (2019) 368–376. doi:10.1016/j.jmst.2018.09.065.

[19] Y.J. Liu, S.J. Li, H.L. Wang, W.T. Hou, Y.L. Hao, R. Yang, T.B. Sercombe, L.C. Zhang, Microstructure, defects and mechanical behavior of beta-type titanium porous structures manufactured by electron beam melting and selective laser melting, Acta Mater. 113 (2016) 56–67. doi:10.1016/j.actamat.2016.04.029.

[20] Y.J. Liu, J.S. Zhang, X.C. Liu, X. Wu, J.C. Wang, Y.S. Zhang, L.Q. Wang, L.C. Zhang, Non-layer-wise fracture and deformation mechanism in beta titanium cubic lattice structure manufactured by selective laser melting, Mater. Sci. Eng. A. 822 (2021) 141696. doi:10.1016/j.msea.2021.141696.

[21] L. Caprio, A.G. Demir, B. Previtali, Influence of pulsed and continuous wave emission on melting

efficiency in selective laser melting, J. Mater. Process. Technol. 266 (2019) 429–441. doi:10.1016/j.jmatprotec.2018.11.019.

[22] A.G. Demir, L. Mazzoleni, L. Caprio, M. Pacher, B. Previtali, Complementary use of pulsed and continuous wave emission modes to stabilize melt pool geometry in laser powder bed fusion, Opt. Laser Technol. 113 (2019) 15–26. doi:10.1016/j.optlastec.2018.12.005.

[23] A.G. Demir, B. Previtali, Additive manufacturing of cardiovascular CoCr stents by selective laser melting, Mater. Des. 119 (2017) 338–350. doi:10.1016/j.matdes.2017.01.091.

[24] V. Finazzi, A.G. Demir, C.A. Biffi, C. Chiastra, F. Migliavacca, L. Petrini, B. Previtali, Design Rules for Producing Cardiovascular Stents by Selective Laser Melting: Geometrical Constraints and Opportunities, Procedia Struct. Integr. 15 (2019) 16–23. doi:10.1016/j.prostr.2019.07.004.

[25] V. Finazzi, A.G. Demir, C.A. Biffi, F. Migliavacca, L. Petrini, B. Previtali, Design and functional testing of a novel balloon-expandable cardiovascular stent in CoCr alloy produced by selective laser melting, J. Manuf. Process. 55 (2020) 161–173. doi:10.1016/j.jmapro.2020.03.060.

[26] D. Carluccio, A.G. Demir, L. Caprio, B. Previtali, M.J. Bermingham, M.S. Dargusch, The influence of laser processing parameters on the densification and surface morphology of pure Fe and Fe-35Mn scaffolds produced by selective laser melting, J. Manuf. Process. 40 (2019) 113–121. doi:10.1016/j.jmapro.2019.03.018.

[27] E. Onal, A.E. Medvedev, M.A. Leeflang, A. Molotnikov, A.A. Zadpoor, Novel microstructural features of selective laser melted lattice struts fabricated with single point exposure scanning, Addit. Manuf. 29 (2019) 100785. doi:10.1016/j.addma.2019.100785.

[28] S. Ghouse, S. Babu, R.J. Van Arkel, K. Nai, P.A. Hooper, J.R.T. Jeffers, The influence of laser parameters and scanning strategies on the mechanical properties of a stochastic porous material, Mater. Des. 131 (2017) 498–508. doi:10.1016/j.matdes.2017.06.041.

[29] S. Tsopanos, R.A.W. Mines, S. McKown, Y. Shen, W.J. Cantwell, W. Brooks, C.J. Sutcliffe, The influence of processing parameters on the mechanical properties of selectively laser melted stainless steel microlattice structures, J. Manuf. Sci. Eng. Trans. ASME. 132 (2010) 0410111–04101112. doi:10.1115/1.4001743.

[30] H. Korn, P. Koch, R. Kordaß, C. Schöne, B. Müller, S. Holtzhausen, Influences of Scan Strategy and Exposure Parameters on Diameter and Surface Quality of Struts in Lattice Structures, in: 2018: pp. 1–7.

[31] A.G. Demir, P. Colombo, B. Previtali, From pulsed to continuous wave emission in SLM with contemporary fiber laser sources: effect of temporal and spatial pulse overlap in part quality, Int. J. Adv. Manuf. Technol. 91 (2017) 2701–2714. doi:10.1007/s00170-016-9948-7.

[32] A.G. Demir, B. Previtali, N. Lecis, Development of laser dimpling strategies on TiN coatings for tribological applications with a highly energetic Q-switched fibre laser, Opt. Laser Technol. 54 (2013) 53–61. doi:10.1016/j.optlastec.2013.05.007.

[33] L. Caprio, A.G. Demir, B. Previtali, Comparative study between CW and PW emissions in selective laser melting, J. Laser Appl. 30 (2018) 032305. doi:10.2351/1.5040631.

[34] Y. Li, P. Pavanram, J. Zhou, K. Lietaert, P. Taheri, W. Li, H. San, M.A. Leeflang, J.M.C. Mol, H. Jahr, A.A. Zadpoor, Additively manufactured biodegradable porous zinc, Acta Biomater. 101 (2020) 609–623. doi:10.1016/j.actbio.2019.10.034.

[35] Y. Qin, P. Wen, M. Voshage, Y. Chen, P.G. Schückler, L. Jauer, D. Xia, H. Guo, Y. Zheng, J.H. Schleifenbaum, Additive manufacturing of biodegradable Zn-xWE43 porous scaffolds: Formation quality, microstructure and mechanical properties, Mater. Des. 181 (2019) 107937. doi:10.1016/j.matdes.2019.107937.

[36] G. Catalano, A.G. Demir, V. Furlan, B. Previtali, Prototyping of biodegradable flat stents in pure zinc by laser microcutting and chemical etching, J. Micromechanics Microengineering. 28 (2018) 095016.

doi:10.1088/1361-6439/aac83d.

[37] E. Mostaed, M. Sikora-Jasinska, A. Mostaed, S. Loffredo, A.G. Demir, B. Previtali, D. Mantovani, R. Beanland, M. Vedani, Novel Zn-based alloys for biodegradable stent applications: Design, development and in vitro degradation, J. Mech. Behav. Biomed. Mater. 60 (2016) 581–602. doi:10.1016/j.jmbbm.2016.03.018.

[38] R.H. Galib, A. Sharif, Development of Zn-Mg Alloys as a Degradable Biomaterial, Columbia Int. Publ. Adv. Alloy. Compd. 1 (2016) 1–7. doi:10.7726/aac.2016.1001.

[39] L.Q. Wang, Y.P. Ren, S.N. Sun, H. Zhao, S. Li, G.W. Qin, Microstructure, mechanical properties and fracture behavior of As-extruded Zn-Mg binary alloys, Acta Metall. Sin. (English Lett. 30 (2017) 931–940. doi:10.1007/s40195-017-0585-4.

[40] Y. Qin, P. Wen, D. Xia, H. Guo, M. Voshage, L. Jauer, Y. Zheng, J.H. Schleifenbaum, Y. Tian, Effect of grain structure on the mechanical properties and in vitro corrosion behavior of additively manufactured pure Zn, Addit. Manuf. 33 (2020) 101134. doi:10.1016/j.addma.2020.101134.

[41] S. Mckown, Y. Shen, W.K. Brookes, C.J. Sutcliffe, W.J. Cantwell, G.S. Langdon, The quasi-static and blast loading response of lattice structures, 35 (2008) 795–810. doi:10.1016/j.ijimpeng.2007.10.005.

[42] D. Vojtěch, J. Kubásek, J. Šerák, P. Novák, Mechanical and corrosion properties of newly developed biodegradable Zn-based alloys for bone fixation, Acta Biomater. 7 (2011) 3515–3522. doi:10.1016/j.actbio.2011.05.008.

[43] M. Leary, M. Mazur, H. Williams, E. Yang, A. Alghamdi, B. Lozanovski, X. Zhang, D. Shidid, L. Farahbod-sternahl, G. Witt, I. Kelbassa, P. Choong, M. Qian, M. Brandt, Inconel 625 lattice structures manufactured by selective laser melting ( SLM ): Mechanical properties , deformation and failure modes, Mater. Des. 157 (2018) 179–199. doi:10.1016/j.matdes.2018.06.010.

[44] E. Mostaed, M. Sikora-Jasinska, A. Mostaed, S. Loffredo, A.G. Demir, B. Previtali, D. Mantovani, R. Beanland, M. Vedani, Novel Zn-based alloys for biodegradable stent applications: Design, development and in vitro degradation, J. Mech. Behav. Biomed. Mater. 60 (2016) 581–602. doi:10.1016/j.jmbbm.2016.03.018.

[45] M. Anilli, A.G. Demir, B. Previtali, Additive manufacturing of laser cutting nozzles by SLM: processing, finishing and functional characterization, Rapid Prototyp. J. 24 (2018) 562–583. doi:10.1108/RPJ-05-2017-0106.

[46] S. Bagherifard, N. Beretta, S. Monti, M. Riccio, M. Bandini, M. Guagliano, On the fatigue strength enhancement of additive manufactured AlSi10Mg parts by mechanical and thermal post-processing, Mater. Des. 145 (2018) 28–41.

[47] L.J. Gibson, Mechanical behavior of metallic foams, Annu. Rev. Mater. Sci. 30 (2000) 191–227. doi:10.1146/annurev.matsci.30.1.191.

[48] M.F. Ashby, The properties of foams and lattices, Philos. Trans. R. Soc. A Math. Phys. Eng. Sci. 364 (2006) 15–30. doi:10.1098/rsta.2005.1678.

[49] T. Maconachie, M. Leary, B. Lozanovski, X. Zhang, M. Qian, O. Faruque, M. Brandt, SLM lattice structures: Properties, performance, applications and challenges, Mater. Des. 183 (2019) 108137. doi:10.1016/j.matdes.2019.108137.

[50] D.C. Montgomery, Design and analysis of experiments, John Wiley & Sons, 2017.

[51] X. Zheng, H. Lee, T.H. Weisgraber, M. Shusteff, J. DeOtte, E.B. Duoss, J.D. Kuntz, M.M. Biener, Q. Ge, J.A. Jackson, S.O. Kucheyev, N.X. Fang, C.M. Spadaccini, Ultralight, ultrastiff mechanical metamaterials, Science (80-. ). 344 (2014) 1373–1377. doi:10.1126/science.1252291.

[52] E. Alabort, D. Barba, R.C. Reed, Design of metallic bone by additive manufacturing, Scr. Mater. 164

(2019) 110–114. doi:10.1016/j.scriptamat.2019.01.022.

[53] D. Jafari, W.W. Wits, T.H.J. Vaneker, A.G. Demir, B. Previtali, B.J. Geurts, I. Gibson, Pulsed mode selective laser melting of porous structures: Structural and thermophysical characterization, Addit. Manuf. 35 (2020) 101263. doi:10.1016/j.addma.2020.101263.

## List of tables

Table 1. Chemical composition analysis results by the powder supplier and by EDS measurements

Table 2. Main specification of the LPBF system employed

Table 3. Fixed and variable factors of experimental campaign

Table 4. Overview of the literature results compared with the ones of the present research and with the reference values for bone scaffolds (* data are extrapolated from plots)

## List of figures

Figure 1. Schematic representation of the single pulse interaction

Figure 2. Centroid-defined single point exposure applied to the manufacturing of a porous bone scaffold with BCC lattice unitary cell (*c* is the unitary cell dimension).

Figure 3. (a) SEM image of the powder, (b) metallographic cross section of the particles and (c) PSD estimated using the Circular Equivalent Diameter volume distribution

Figure 4. CAD models of the BCC lattices with tilted and frontal views: (a) and (e) cubical with *c*=1 mm, (b) and (f) cubical with *c*=2 mm, (c) and (g) cylindrical with *c*=1 mm, and (d) and (h) cylindrical with *c*=2 mm

Figure 5. (a) Top view SEM image, (b) metallographic cross section of a sample, (c) micro-CT acquisition and (d) strut diameter measurement.

Figure 6. Photodiode acquisitions for (a) P=15 W, (b) P=40 W, and (c) P=65 W. (d) Measurements carried out on a signal. (e) The measured rise and (e) fall times against the power levels. (f) Measured pulse duration against the commanded $t_{on}$.

Figure 7. Macro images of the cubical samples attached to the build plate

Figure 8. (a) SEM top images of a representative condition for each combination of the process parameters and (b) results of the dimensional characterization of the strut diameter. Dashed line depict trend, while the error bars show standard deviation. (BD: build direction)

Figure 9. Metallographic cross-sections acquired through optical microscopy of a representative condition for each combination of the process parameters (BD: build direction).

Figure 10. Results of the relative density measurements (dashed lines depict trend).

Figure 11. Results from the EDS measurements performed on the lattice samples, compared with reference EDS measurements on powder and with the declared powder composition as provided by the supplier. Error bars show standard deviation. (UL=Upper Limit, LL=Lower Limit)

Figure 12. Typical microstructure of Zn-0.5Mg lattice taken at the scan plane at low magnification (a) and high magnification (b)

Figure 13. (a) Stress ($\sigma$) - strain ($\varepsilon$) curves of the produced lattices with $c$=1 mm. (b) Macro images of the samples after compression testing.

Figure 14. Overview of the mechanical properties obtained for lattices with $c$=1 mm, (a) compressive yield strength, (b) compressive strength, (c) Young's modulus, (d) strain at failure. Dashed line depict trend, while the error bars show standard deviation.

Figure 15. SEM images of the fracture surfaces: (a) showing fracture locations, (b) higher magnification on the detail highlighted in the previous image and (c) high magnification image showing transgranular brittle fracture

Figure 16. $\sigma^*\sigma_{y,s}$ as a function of $\rho^*\rho_s$ with the fitted Gibbs-Ashby model. The shaded regions represent the 95% confidence intervals for the fits. The regression coefficients are given separately for the two different power levels with their 95% confidence intervals.

Figure 17. Implant mock-up positioned as a filling scaffold for the a jawbone defect.